A New Surface Model for Cyclone–Anticyclone Asymmetry

Gregory J. Hakim[1], Chris Snyder[2], and David J. Muraki[3]

[1] University of Washington, Seattle, WA, USA

[2] National Center for Atmospheric Research, Boulder, CO, USA

[3] Simon Fraser University, Burnaby, BC, Canada

Submitted to *Journal of the Atmospheric Sciences*

February 27, 2002

[1]Corresponding Author: Gregory J. Hakim, Department of Atmospheric Sciences, Box 351640, University of Washington, Seattle, WA 98195-1640; e-mail: hakim@atmos.washington.edu

Abstract

Cyclonic vortices on the tropopause are characterized by compact structure and larger pressure, wind and temperature perturbations when compared to broader and weaker anticyclones. Neither the origin of these vortices nor the reasons for the preferred asymmetries are completely understood; quasigeostrophic dynamics, in particular, have cyclone–anticyclone symmetry.

In order to explore these and related problems, we introduce a novel small Rossby-number approximation to the primitive equations applied to a simple model of the tropopause in continuously stratified fluid. This model resolves dynamics that give rise to vortical asymmetries, while retaining both the conceptual simplicity of quasigeostrophic dynamics and the computational economy of two-dimensional flows. The model contains no depth-independent (barotropic) flow, and thus may provide a useful comparison to two-dimensional flows dominated by this flow component.

Solutions for random initial conditions (i.e., freely decaying turbulence) exhibit vortical asymmetries typical of tropopause observations, with strong localized cyclones, and weaker diffuse anticyclones. Cyclones cluster around a distinct length scale at a given time whereas anticyclones do not. These results differ significantly from previous studies of cyclone–anticyclone asymmetry in the shallow-water primitive equations and the periodic balance equations. An important source of asymmetry in the present solutions is divergent flow associated with frontogenesis and the forward cascade of tropopause potential-temperature variance. This thermally direct flow changes the mean potential temperature of the tropopause, selectively maintains anticyclonic filaments relative to cyclonic filaments, and appears to promote merger of anticyclones relative to cyclones.

1. Introduction

Observations of vortical disturbances in the extratropics reveal structural and population asymmetries between cyclones and anticyclones from the mesoscale to the planetary scale. An example of these asymmetries is given by mesoscale undulations of the tropopause. Tropopause vortices have typical radii of approximately 500 km, with cyclones characterized by larger pressure, wind and temperature perturbations when compared to anticyclones (Thorpe 1986; Hakim 2000; Muraki and Hakim 2001; Wirth 2001). Moreover, cyclones typically have compact structure when compared with broader anticyclones. Neither the origin of these vortices nor the reasons for the preferred structural asymmetries are completely understood. Here we explore these problems using a novel small Rossby-number approximation to the primitive equations (PE) applied to a simple model of the tropopause. This model resolves the balanced dynamics that give rise to vortical asymmetries, such as vortex stretching of relative vorticity and divergence–vorticity feedbacks associated with frontogenesis. Moreover, the model retains the conceptual simplicity of quasigeostrophic dynamics (QG) and the computational economy of two-dimensional dynamics.

One hypothesis for the origin of tropopause vortices derives from numerical solutions showing spontaneous vortex emergence from random initial conditions in unforced quasi-two-dimensional flows (e.g., McWilliams 1984; McWilliams 1990a,b; Bracco et al. 2000). Studies of random initial conditions are particularly useful with regard to cyclone–anticyclone asymmetry because they allow preferred structures to be selected by the dynamics. An indirect suggestion of the turbulence hypothesis is contained within Sanders' (1988) observational study on the origin of tropopause disturbances: "Evidently, the organization and growth of the system out of the small-scale chaos of the vorticity field is the most important process." Although purely two-dimensional (barotropic vorticity) dynamics may lend support to a turbulent-cascade hypothesis for the origin of vortices, these dynamics do not resolve cyclone–anticyclone asymmetry.

The simplest three-dimensional representation of the tropopause in continuously stratified fluid consists of a quasi-horizontal interface separating regions of homogeneous potential vorticity (PV) of differing magnitude; small (large) values of PV are located on the tropospheric (stratospheric) side of the interface (Rivest et al. 1992; Juckes 1994; Muraki and Hakim 2001). The QG approximation to this configuration results in a profound simplification that parallels the dynamics of the barotropic vorticity equation: the three dimensional flow is modeled entirely by horizontal advection of potential temperature on the interface (Blumen 1978; Juckes 1994; Held et al. 1995). Following Held et al. (1995), we shall refer to this approximation as "surface quasigeostrophy" (sQG). An interesting attribute of sQG is the absence of depth-independent (barotropic) flow; as such, it provides a useful comparison to two-dimensional flows dominated by this flow component. For completeness, we also note that because the sQG assumption requires zero PV gradients away from the interface, Rossby-wave propagation is confined to the interface and baroclinic instability is excluded.

Although sQG dynamics resolve the emergence of vortices out of random initial conditions, they fail to produce cyclone–anticyclone asymmetry. Here we allow for cyclone–anticyclone asymmetry by extending sQG by one order in Rossby number ("sQG^{+1}") as in Muraki et al. (1999), which includes additional dynamics such as ageostrophic advections, stretching and tilting of relative vorticity, and gradient-wind effects (centripetal accelerations). Although the model is applied here to specific problems related to the tropopause, we emphasize that it applies to a more-general class of problems characterized by balanced dynamics and uniform potential vorticity.

Cyclone–anticyclone asymmetry and vortex emergence from random initial conditions have also been explored numerically for other dynamical systems more complete than QG. For example, Cushman-Roisin and Tang (1990) observed a strong bias for anticyclones in a generalized geostrophic model. A subsequent study by Polvani et al. (1994) using the shallow-water PE also found that anticyclones were the preferred vortical structures. A

similar result has been found for three-dimensionally periodic solutions of the balance equations (Yavneh et al. 1997). These results stand in contrast to the observed preference for tropopause cyclones, and motivate the present investigation into the importance of PV dynamics concentrated at an interface as compared to deep distributions over a layer.

A representative sample of the main results to be documented in this paper is given in Fig. 1. Because the solutions decay away from the interface, tropopause dynamics (downward decay) may also be modeled as surface dynamics (upward decay) with the only difference being that cyclones are associated with cold (warm) air on the tropopause (surface). Here and for the remainder of the paper we move from the tropopause to the surface. A random distribution of surface potential temperature (Fig. 1a) rapidly evolves into a field of coherent vortices and a region between the vortices filled by incoherent warm and cold filaments (Figs. 1b–d). By $t = 1000$ (nondimensional time units), the sQG^{+1} solution exhibits distinct cyclone–anticyclone asymmetries in both vortex population number and structure that are absent in the sQG solution (cf. Figs. 1c,d). In terms of population number, cyclones (warm spots) appear to cluster around a distinct length scale, whereas anticyclones (cold spots) do not. In terms of vortex structure, cyclones possess a "plateau" structure with sharply defined edges, whereas anticyclones possess broadly distributed structure with poorly defined edges (Fig. 1c). Another striking property of the sQG^{+1} solution is the blue background, which indicates a mean cooling of the surface has occurred (Figs. 1b,c); the cooling rate is greatest at early times and then decays slowly with time (Fig. 2a). In the sQG^{+1} potential-temperature probability-density function (PDF), surface cooling appears as a shifted peak and is bias toward cold values for small potential temperature, relative to the sQG PDF (Fig. 2b). As we will show, surface cooling is due to divergence–vorticity feedbacks associated with frontogenesis, such that over time, warm air rises and cold air sinks. This realistic feedback is also crucial to the vortex asymmetries, and is absent in two-dimensional and shallow-water dynamics.

The remainder of the paper is organized as follows. Section 2 provides a brief background discussion of quasi-two-dimensional turbulence relevant to the present work. Section 3 is devoted to defining the new surface model, sQG^{+1}, along with a description of the numerical algorithm. Novel aspects of the solution shown in Fig. 1, surface cooling and cyclone–anticyclone asymmetries, are documented in sections 4 and 5, respectively. A summary is given in section 6, along with several hypotheses to be tested in future research.

2. Background on Quasi-Two-Dimensional Turbulence

This section is dedicated to providing a brief background review of certain aspects of quasi-two-dimensional turbulence as they apply to the present work. Turbulent flows are dominated by nonlinear (inertia) dynamics, significant vorticity, and rapid mixing of passive tracers (e.g., Salmon 1998; section 4.5). An important property of nonlinear dynamics is a propensity to spectrally scatter fluid properties, such as energy and enstrophy, in preferred directions (e.g., to larger or smaller scales). At length scales well removed from significant forcing and dissipation, this nonlinear scattering may take the form of statistically steady cascades. In three-dimensional turbulence, for example, energy cascades toward shorter length scales on the way to molecular dissipation.

Two-dimensional turbulence differs from three-dimensional turbulence because it conserves enstrophy (for weak dissipation) and thus supports two cascades: an upscale cascade of energy, and a downscale cascade of enstrophy. A kinematic explanation for the downscale cascade is formed around the fact that the area contained within closed contours of vorticity is conserved, so that vorticity gradients increase as patches of fluid inevitably distort from axisymmetry. For statistically steady cascades, the energy spectrum has a k^{-3} power law for the downscale enstrophy cascade, and a $k^{-5/3}$ power law for the upscale energy cascade, where k is the total wavenumber (e.g., Salmon 1998, section 4.9).

Charney (1971) asserts that the two-dimensional inertial-range predictions also apply to unbounded three-dimensional QG dynamics when enstrophy is replaced by potential en-

strophy; i.e., PV cascades to small scales. The effect of rigid horizontal boundaries in the QG system has been studied by Blumen (1978), Juckes (1994), and Held et al. (1995) for uniform PV above a flat boundary with nonuniform potential-temperature distribution (i.e., the sQG system). If dissipation is weak, boundary potential-temperature variance cascades downscale with a $k^{-5/3}$ spectrum for equilibrium conditions. This cascade is analogous to the enstrophy cascade of two-dimensional turbulence, and is characterized by increasing potential temperature gradients as material lines are deformed and elongated. The upscale energy cascade has a k^{-1} spectrum in potential-temperature variance.

Fig. 3 shows the ensemble-mean potential-temperature variance spectrum for sQG and sQG^{+1} solutions at $t = 1000$. The spectra do not match the k^{-1} and $k^{-5/3}$ power laws because these freely decaying (unforced) simulations do not achieve statistical equilibrium. Furthermore, we note that steeper spectral slopes in the forward cascades of turbulent flows are also associated with the emergence of highly organized and coherent vortical structures that disrupt the cascades (e.g., Lumley 1990). In quasi-two-dimensional (i.e., two-dimensional QG and sQG) freely decaying turbulence, these vortices emerge spontaneously from random initial conditions, and represent patches of organized vorticity within a field of disorganized, thin, filaments of vorticity (e.g., McWilliams 1984). Vortices of like sign typically merge, producing larger vortices that then undergo an axisymmetrization process where filaments are shed and dissipated outside a persistent axisymmetric vortex core. The generation and dissipation of filaments represents the forward enstrophy cascade to dissipation scales, whereas the scale increase of the vortices is a manifestation of the upscale energy cascade.

Vortex emergence and evolution properties for sQG turbulence are qualitatively similar to those for two-dimensional turbulence, although they have not been studied as extensively (Held et al. 1995). One important distinction is that sQG filaments tend toward instability as they are thinned (Juckes 1995), which is not observed to occur in two-dimensional turbulence. Held et al. (1995) note that the instability growth rate is set by the magnitude of the filament

vorticity, which remains constant for two-dimensional filaments and increases without bound for thinning potential-temperature filaments. An additional distinction is that the inversion from potential temperature to streamfunction is more local than the inversion from vorticity to streamfunction, so that vortex interactions decrease more rapidly with distance for sQG dynamics.

Changing the sign of the initial condition in two-dimensional, QG, and sQG turbulence simply changes the sign of the solution. This property results in vortices and filaments that are symmetric; there is no dynamical distinction between cyclones and anticyclones. This symmetry is broken by systems that retain dynamically active divergent flow or PV inversions more accurate than QG, such as the shallow-water PE and the balance equations. Specifically, Polvani et al. (1994) find that anticyclones are preferred over cyclones in shallow-water flow as the Froude number (ratio of fluid speed to gravity-wave speed) increases. Yavneh et al. (1997) show that anticyclones also dominate in three-dimensional periodic f-plane simulations of the balance equations. In particular, anticyclones develop rapidly to larger horizontal scales, as in shallow water, which allows them to interact over deeper layers and vertically align into columnar vortices faster than cyclones.

The strong bias for anticyclones in the shallow-water PE and periodic balance equations stands in contrast to the observed cyclonic bias at the tropopause. In order to resolve this discrepancy, a new model that extends sQG is proposed and applied to an idealized representation of the tropopause. The essential novel additions to sQG dynamics are asymptotically consistent next-order rotational and divergent winds. We anticipate that the cascade of potential-temperature variance to small scales will provoke a divergent response that also affects the rotational flow.

3. A New Surface Model: sQG^{+1}

We begin with a description of a new surface model that is a balance approximation of the PE, followed by a description of the numerical procedure and a discussion on dissipation.

The tropopause is approximated here as an interface separating regions of homogeneous PV of differing value (Rivest et al. 1992; Juckes 1994; Muraki and Hakim 2001). Although in general the interface position is a function of space and time, for simplicity we shall take the interface to be a rigid surface (equivalent to assuming infinite PV on one side of the interface). Moreover, we "invert" the tropopause such that disturbances decay upward rather than downward from the the rigid interface; this choice merely reverses the sign of warm and cold anomalies.

We are interested in balanced motions supported by the Boussinesq, hydrostatic, f-plane, PE in the assumed geometry. Balanced motions are defined here as those that satisfy both balanced dynamics and a balance condition, which renders the dynamics free of gravity waves (Warn et al. 1995; Vallis 1996). Balanced dynamics may be represented by the material conservation of Ertel PV, q, in the interior ($z > 0$),

$$\frac{Dq}{Dt} \;=\; \mathcal{D}^q q \;, \tag{1}$$

and potential temperature, θ, on the rigid boundary ($z = 0$),

$$\frac{D\theta^s}{Dt} \;=\; \mathcal{D}^\theta \theta^s. \tag{2}$$

The perturbation PV is defined in terms of the primitive variables (u, v, θ) by

$$q \;=\; \{v_x - u_y + \theta_z\} + \epsilon \left\{(v_x - u_y)\,\theta_z - v_z\,\theta_x + u_z\,\theta_y\right\} \;, \tag{3}$$

and θ is a perturbation from a constant-stratification reference state. Subscripts denote partial derivatives, superscript s indicates a surface value ($z = 0$), $\mathcal{D}^q$ and $\mathcal{D}^\theta$ are dissipation operators, and

$$\frac{D}{Dt} \equiv \frac{\partial}{\partial t} + u\,\frac{\partial}{\partial x} + v\;\frac{\partial}{\partial y} + \epsilon w\;\frac{\partial}{\partial z} \tag{4}$$

is the material derivative for wind vector $\vec{V} = (u, v, w)$. The vertical coordinate, z, is pseudo-height (Hoskins and Bretherton 1972), and ϵ is the Rossby number. All variables have been

non-dimensionalized as in Pedlosky (1987; Chapter 6), with the exception that w is scaled by an additional factor of ϵ.

For homogeneous q, which we take to be zero, the interior equation (1) is satisfied exactly. This condition reduces the dynamics to (2) with $w = 0$; i.e., horizontal advection of surface potential temperature. Despite a reduction to surface advection, the general problem is still three dimensional, because the surface winds (u^s, v^s) are determined by a three-dimensional PV inversion. Here we shall assume small ϵ and treat the balance condition asymptotically following the procedure outlined in Muraki et al. (1999). The advecting winds are then given asymptotically by

$$(u^s, v^s) \;=\; (u^{s0} \,+\, \epsilon u^{s1},\; v^{s0} \,+\, \epsilon v^{s1}) \,+\, O(\epsilon^2). \tag{5}$$

An overview of the principal results of the inversion follows, with further details provided in Appendix A.

The leading-order balance condition yields a standard QG PV inversion for the leading-order geopotential, Φ^0:

$$q^0 = \Phi^0_{xx} + \Phi^0_{yy} + \Phi^0_{zz} \;=\; 0; \qquad\qquad \Phi^0_z(z=0) \;=\; \theta^s. \tag{6}$$

Taking a Fourier transform and choosing decay in the upward direction, a solution is

$$\hat{\Phi}^0(k,l) \;=\; -\frac{\hat{\theta}^s(k,l)}{|K|}\; e^{-|K|z}, \tag{7}$$

where hats denote spectral variables, k and l are x and y wavenumbers, and $|K| = (k^2+l^2)^{1/2}$. Leading-order (QG) winds are then determined by an inverse Fourier transform of spectral winds given by $(\hat{u}^0, \hat{v}^0) = (-ik\,\hat{\Phi}^0,\; il\,\hat{\Phi}^0)$. The sQG system is defined by (7) and (2), when the advecting wind (u^s, v^s) is approximated by (u^{s0}, v^{s0}) (Held et al. 1995; Juckes 1994). A noteworthy attribute of this system is the dimensional reduction that allows the solution of a three-dimensional flow by a two-dimensional computation.

The next-order balance condition yields corrected winds $(u^{s0} + \epsilon u^{s1}, v^{s0} + \epsilon v^{s1})$ that, together with (2), define the sQG^{+1} system. For the present discussion, two important

aspects of the next-order calculation deserve mention here. First, the corrections have the remarkable property that, despite the three-dimensional nature of the inversion problem, (u^{s1}, v^{s1}) are determined entirely from a surface calculation based on θ^s; this again reduces the full three-dimensional calculation to a surface problem. Second, although the leading-order winds are strictly nondivergent, the corrections possess both divergence and vorticity. The nondivergent corrections include those due to (approximate) gradient-wind balance, while the irrotational corrections are secondary circulations and vertical motion that are driven by frontogenesis in the leading-order flow.

3.1 Numerics

The numerical solution method consists of two steps, inversion and advection. Inversion involves recovering $u^s \sim u^{s0} + \epsilon u^{s1}$ and $v^s \sim v^{s0} + \epsilon v^{s1}$ from θ^s as described above. These approximate winds are then used to advect θ^s in (2). We represent the dissipation operators by eighth-order horizontal "hyperdiffusion" (e.g., McWilliams 1984),

$$\mathcal{D}^\theta \;=\; \mathcal{D}^q \;=\; -\nu \nabla_{\!H}^{8}, \tag{8}$$

where ${\nabla_{\!H}}^2 = \partial_{xx} + \partial_{yy}$. As discussed further in the subsequent section, this representation for dissipation has little connection to real physics in the PE, and is used in computations to prevent the accumulation of energy at the smallest scales.

Using the dissipation operator specified in (8), a Fourier transform, $\mathcal{F}$, of (2) gives the spectral form of the governing equation that is solved numerically:

$$\frac{\partial \hat{\theta}}{\partial t} \;=\; \mathcal{F}\left[u^s \, \frac{\partial \theta^s}{\partial x} \;-\; v^s \, \frac{\partial \theta^s}{\partial y} \right] \;-\; \nu (k^2 + l^2)^4 \, \hat{\theta}^s. \tag{9}$$

In the numerical model, nonlinear terms in (9) are quadratically de-aliased to a resolution of 512 by 512 horizontal wavenumbers, the Rossby number is $\epsilon = 0.1$, and hyperdiffusion is handled explicitly with $\nu = 10^{-9}$. Temporal discretization is by a third-order accurate Adams–Bashforth scheme (Durran 1999). An ensemble of 25 solutions is employed for both sQG and sQG^{+1} computations to ensure statistically robust results.

Initial conditions are constructed by first specifying a $\hat{\Phi}^0$ field, and then solving for next-order corrections. The $\hat{\Phi}^0$ field is specified with random phase angles and amplitude given by (Polvani et al. 1994)

$$\hat{\Phi}^0_s(k,l) \equiv \frac{|K|^{m/4-1}}{(|K|+k_0)^{m/2}}, \tag{10}$$

on a domain taken to be $2\pi k_0$ square. This definition for $\hat{\Phi}^0$ gives a kinetic-energy spectrum for surface flow peaked at wavenumber k_0. To maintain the kinetic-energy spectrum at next order, the inversions at next order must have no wind corrections. Therefore, the next-order inversions are performed with boundary conditions that provide $(u^{s1}, v^{s1}) = 0$, which forces the corrections into the θ^s field. The initial field is then normalized to have unit total kinetic energy and zero mean potential temperature at $z = 0$. Test solutions for initial conditions in which the θ^s corrections are chosen to be zero and the winds are corrected show no qualitative difference from the control solutions. Following Polvani et al. (1994), we set $k_0 = 14$ and $m = 25$, which gives initial conditions such as the one shown in Fig. 1a.

3.2 Role of Dissipation

Some form of dissipation is required in the numerical experiments to control the build up of grid-scale features associated with the forward cascade of θ^s variance. Our use of hyperdiffusion to dissipate both θ^s and q follows common practice in studies of quasi-two-dimensional turbulence. The fact that q remains constant with such dissipation is particularly useful here (and in sQG studies such as Held at al. 1995), since the calculations become effectively two dimensional, and thus computationally tractable, only when q is constant.

However, for the PE, which sQG^{+1} approximates, most obvious forms of momentum and potential-temperature dissipation result in nonzero time tendency of q even for q constant; that is, an initially uniform field of q will develop spatial variations as a consequence of the dissipation of momentum and potential temperature (e.g., Herring et al. 1994). This effect can be ignored at the level of QG theory[1] but enters at next order in ϵ. Our solution proce-

[1]The QG PV is linear, and if heat and momentum are dissipated by diffusion (or hyperdiffusion), then QG PV is also diffused.

dure, which depends on the assumption of constant q, neglects this dissipation contribution to the time tendency of q.

The importance of this neglected PV to the long-term behavior of the flow is an interesting question that deserves further investigation. Considering the approximations required to reduce the PE to other quasi-two-dimensional systems (e.g., the shallow water equations), we suspect that neglecting some of the dissipative effects on PV is a comparatively minor simplification. Test solutions for changes in the hyperdiffusion coefficient by an order of magnitude showed no qualitative changes to our primary conclusions. Moreover, the key mechanisms that generate asymmetries rely on advections by the divergent flow component, which operate even in the absence of dissipation.

4. Surface Cooling

Surface cooling[2] is one of the novel features of sQG^{+1} turbulence shown in Figs. 1 and 2. This section further documents surface cooling and provides a simple explanation of why this phenomenon occurs. A useful starting point is the equation governing the time-tendency of surface-mean potential temperature, $\bar{\theta}^s$, which is obtained by area-averaging (2) with (8) over the entire surface:

$$\frac{\partial \bar{\theta}^s}{\partial t} = \overline{\left[\theta^s \, \nabla_H \cdot \vec{V}\right]}. \tag{11}$$

Note that the evolution of $\bar{\theta}^s$ has no explicit dependence on hyperdiffusion, and is conserved by the non-divergent leading-order dynamics. However, the next-order dynamics support divergence, and net surface cooling occurs when θ^s and divergence are anticorrelated such that, on average, warm regions contract relative to cold regions.

Since surface divergence (convergence) is associated with sinking (rising) air just above the surface, we conclude that surface cooling is related to rising warm air and sinking cold

[2]Note that the cooling described here applies to the area-mean potential temperature, not individual air parcels, and is a result of adiabatic motion.

air (thermally direct circulations). Conversely, surface warming is associated with thermally indirect circulations, and appears to occur in vortex cores (compare the sQG^{+1} and sQG θ^s PDFs for large $|\theta^s|$ in Fig. 2b). In our balanced model, these circulations are due to frontogenesis, which is defined as an increase in the magnitude of the horizontal potential-temperature gradient following fluid particles.

To understand why these circulations have a preferred direction, recall from section 2 that the deformation of potential-temperature contours by the leading-order velocity field leads to an increase in potential-temperature gradients; equivalently, the turbulence cascades potential-temperature variance from large to small scales. To maintain thermal-wind balance, frontogenesis requires an increase in the vertical shear and therefore the kinetic energy. Since total energy is conserved, this increase in kinetic energy is balanced by a decrease in potential energy through warm air rising and cold air sinking. Although this process occurs at leading order, the divergent flow is diagnostic and does not advect; therefore surface cooling cannot occur for sQG. At next order, sQG^{+1}, divergent flow is dynamically active and may change the area contained within potential temperature contours. Note that this process is consistent with the conservation of potential temperature following fluid particles because the increase in area associated with surface cooling is associated with particles that sink onto the surface. We proceed to test the hypothesis that the main source of frontogenesis, and therefore surface cooling, occurs in the filament field.

To test this hypothesis for surface cooling, we conduct an analysis of kinematic quantities associated with surface frontogenesis: divergence, $u_x + v_y$, and leading-order deformation magnitude, $\left[(u_y^0 + v_x^0)^2 + (u_x^0 - v_y^0)^2\right]^{1/2}$. As an aid in interpreting Fig. 4, we note that most vortices are characterized by relatively large values of $|\,\theta^s - \bar{\theta}^s|$, while most filaments are found where $|\,\theta^s - \bar{\theta}^s|$ is relatively small (cf. Fig. 1); hereafter take $|\,\theta^s - \bar{\theta}^s| \gtrapprox 2$ to represent the vortex field. The largest contributions to the ensemble-mean total-deformation magnitude occur in the filament field near the PDF peak of $\theta^s - \bar{\theta}^s$. A divergence dipole flanks the

$\theta^s - \bar{\theta^s}$ distribution peak, with divergence (convergence) found in relatively cold (warm) air. We conclude that an asymmetry exists in the filament field due to divergent circulations associated with frontogenesis such that, on average, warm air rises away from the surface and cold air sinks toward the surface.

Further evidence of this filament asymmetry is apparent in PDFs of $\theta^s - \bar{\theta^s}$ and vorticity at $t = 1000$. The $\theta^s - \bar{\theta^s}$ ensemble-mean PDF shows a cold bias in the filament field and a warm bias in the vortex field (Fig. 5a). The sQG^{+1} vorticity PDF (Fig. 5b) shows that large values of cyclonic (anticyclonic) vorticity occur more (less) frequently than in sQG, as one might expect based on stretching of relative vorticity. Joint PDFs of vorticity and θ^s show that the large values of cyclonic vorticity occur in the vortex field and that the anticyclonic bias at small values of vorticity occurs in the filament field (Fig. 5c,d).

These results demonstrate the existence of a pronounced cold–anticyclonic bias in the sQG^{+1} filament field; this bias has no counterpart in the symmetric filament fields of two-dimensional, QG, and sQG turbulence. The key element that was previously missing, but that is included in sQG^{+1} is advection by the divergent flow. Thinning warm filaments are accompanied by rising motion and convergence along the filament, which accelerates the thinning of the filament, while the situation is reversed for cold filaments where divergence along the filament slows the thinning.[3] As a result of this asymmetry, warm filaments reach small scales sooner and are dissipated more rapidly, so that the observed filaments are predominantly cold. We hypothesize that this basic asymmetry also plays an important role in determining vortex structure and population asymmetries, which are documented in the following section.

[3]We note that because the divergent flow is O(ϵ) it cannot overwhelm the O(1) strain—cold filaments do not expand. A similar result can be derived from semi-geostrophic solutions of two-dimensional filaments in deformation (Davies and Müller 1988).

5. Cyclone–Anticyclone Asymmetries

Figures 1b,c exhibit asymmetries between cyclonic and anticyclonic vortices in terms of both population number and structure. Cyclones appear to cluster around a distinct size at this time, whereas anticyclones do not, and cyclones tend to have a plateau-like structure, whereas anticyclones tend to have a broad, sprawling, structure. This section is devoted to quantifying these qualitative impressions.

Vortices are identified by a census algorithm that is described in Appendix B. For each vortex, the algorithm objectively determines vortex amplitude ($\theta^s - \bar{\theta^s}$ extremum), and major- and minor-axis length scales. Hereafter, radius refers to the vortex major-axis length scale. Vortex population statistics at $t = 1000$ are discussed first, followed by an analysis of the statistics over time, and finally an analysis of vortex structure.

5.1 Vortex census

Histograms of sQG^{+1} ensemble-mean vortex amplitude show that cyclones tend to be stronger than anticyclones, with a mean of 3.27 as compared to -1.5 for anticyclones (Fig. 6a). Anticyclones exhibit a single peak near $\theta^s - \bar{\theta^s} = -1$, whereas cyclones exhibit a bimodal distribution with a primary peak near $\theta^s - \bar{\theta^s} = 4$. Both the anticyclone peak, and the secondary cyclone peak near $\theta^s - \bar{\theta^s} = 1$ are due to thin-filament instability. We suspect that the observation of fewer cyclones relative to anticyclones for small-scales is due to the shorter lifespan of warm filaments in sQG^{+1} strain. The symmetric sQG amplitude histogram also exhibits two peaks for both cyclones and anticyclones, and both distributions are dominated by vortices with small values of $|\theta^s - \bar{\theta^s}|$ (Fig. 6b).

sQG^{+1} anticyclones exhibit no preferred length scale, but rather show an exponential decrease in number away from a peak at small scales; the tail of the distribution reaches to values more than twice as large as for cyclones (Fig. 6c). sQG^{+1} cyclones exhibit two peaks, with one near $r \approx 3$ and another near $r \approx 7$. The symmetric sQG vortex–radius plot is sharply peaked at small scales with a minor secondary peak near $|r| \approx 13$. The primary

peak reflects vortex generation at small scales due to filamentary instability, whereas the secondary peak reflects the upscale cascade due to vortex merger.

Plots of sQG^{+1} vortex radius as a function of amplitude show that the anticyclonic vortex distribution peaks at small amplitudes and small radii with a long tail to large radii at modestly larger amplitude (Fig. 7a). In contrast, cyclones tend to cluster around ($\theta^s - \bar{\theta}^s \approx 4$, $r \approx 7$) with very few cyclones at larger radii. Fewer cyclones occur near the second peak at small amplitude and radius relative to the anticyclone distribution. The asymmetric sQG^{+1} vortex amplitude–radius relationship is steeper (shallower) for anticyclones (cyclones) when compared to the sQG relationship (Fig. 7b). sQG vortices cascade to large scales along an approximately parabolic amplitude–radius relationship, which must asymptote to the $\theta^s - \bar{\theta}^s$ extrema in the initial conditions, because θ^s is conserved following fluid particles.

These instantaneous results suggest that sQG^{+1} anticyclones cascade rapidly to larger scale, whereas sQG^{+1} cyclones appear to "cluster" around a distinct scale. Further evidence for this tendency is given in Fig. 8 which shows the total number of cyclones and anticyclones as a function of time. Relative to the sQG curve, the number of sQG^{+1} cyclones (anticyclones) decreases less (more) with time. Although filamentary instability also contributes to variations in the number of vortices, the asymmetries shown in Figs. 6–8 suggest a difference in how cyclones and anticyclones interact and merge. The summary section provides additional analysis of this vortex-merger asymmetry, and a hypothesized frontogenesis mechanism to explain it.

Fig. 8 also shows that the total number of sQG vortices approximates a $t^{-.55}$ power law. Similar laws have been observed for two-dimensional (McWilliams 1990a; Bracco et al. 2000) and three-dimensional-periodic QG turbulence (McWilliams 1990b; McWilliams et al. 1999), but with steeper power laws of $t^{-.72}$ and $t^{-1.25}$, respectively. A slower decrease in vortex number for sQG dynamics relative to two-dimensional dynamics is consistent with the observation that two-dimensional vortices have a larger range of influence, which may

lead to interaction and merger with other vortices, when compared to sQG vortices. The source of this larger influence may be attributed to the slower spatial decay of the $\ln(r)$ two-dimensional Green's function, when compared to r^{-1} for the sQG Green's function (Held et al. 1995). Because the r^{-1} Green's function also applies to three-dimensional QG dynamics, the source of the difference may be more closely related to surface-based dynamics as compared to deep, barotropic dynamics. Conclusions drawn from Fig. 8 must again be tempered by the caveat that vortex number is changed by filamentary instability, which is largely absent from strictly two-dimensional flows.

5.2 Vortex structure

A structural asymmetry apparent in Fig 1c is the tendency for compact cyclones with sharp edges and broad anticyclones with diffuse edges. An objective measure of this asymmetry is provided by PDFs of cyclonic and anticyclonic $|\nabla_H \theta^s|$ conditioned on $|\theta^s - \bar{\theta^s}| > 1$ (Fig. 9). The sQG^{+1} plot shows that stronger gradients are found in warm air (cyclones), with gradients in cold air (anticyclones) comparable to the sQG result.

A plot of sQG^{+1} vorticity corresponding to the upper-left quadrant of Fig. 1c shows that, as expected, there is considerably more small-scale structure in the vorticity field when compared to the θ^s field (Fig. 10a). The vortex field shows larger vorticity values near cyclones compared to anticyclones. Both cyclones and anticyclones exhibit annular-like vorticity structure in the vortex core, and a tendency toward compensation, with a ring of opposite-sign vorticity surrounding the core; these properties are most noticeable for sQG^{+1} cyclones. Another interesting property is the tendency for small anticyclones to become trapped as satellites with nearly constant orbits around cyclones [see, e.g., $(x, y) = (-40,10)$ in Fig. 10]. Such configurations are observed to last for hundreds of time units (not shown), and stand in contrast to the two-dimensional tendency for irreversible deformation of vortices of unequal amplitude in close proximity[4] (e.g., Guinn and Schubert 1993).

[4]Vortices of opposite sign and comparable amplitude often merge to form vortex dipoles.

The absence of stretching of relative vorticity for sQG dynamics is apparent in the sQG vorticity plot, which shows notably smaller magnitude vorticity relative to sQG^{+1} (Fig. 10b; cf. Fig. 5b). sQG vortices are also compensated, but with less clearly defined rings of vorticity when compared to sQG^{+1} cyclones because the edges of sQG cyclones are not as sharply defined. Moreover, most sQG vortices are nearly axisymmetric, whereas many sQG^{+1} cyclones appear to be elliptical. Last, we note that composite averages of cyclones and anticyclones were not helpful in quantifying structural asymmetries because averaging tends to smooth out the sharp structures that vary in location from vortex to vortex.

6. Summary and Hypotheses

We introduce a new model, sQG^{+1}, which is devised to study the dynamics of continuously stratified fluids characterized by balanced dynamics, uniform potential vorticity, and a rigid boundary. The model builds asymptotically upon surface-QG dynamics (e.g., Held et al. 1995) by including next-order corrections to the leading-order non-divergent velocity field (Muraki et al. 1999). This approach retains conceptually useful QG concepts while also allowing the solution of three-dimensional dynamics with two-dimensional computational effort. We have applied the sQG^{+1} model to the problem of cyclone–anticyclone asymmetry, in order to investigate the observed bias for tropopause cyclones.

We use unbiased random initial conditions, which allows the dynamics to select asymmetries; this is the classic initial-value problem known as "freely decaying" turbulence. Vortices emerge from the turbulence as in two-dimensional simulations; however, there is a distinct dynamical asymmetry favoring strong, compact cyclones and weak, broad anticyclones. Cyclone size clusters around a distinct length scale at a given time, whereas anticyclones do not, and reach scales much larger than cyclones.

The results suggest that as surface potential temperature cascades to small scales, frontogenesis produces divergence that is the source for several asymmetries. As Fig. 11 illustrates, a basic asymmetry occurs at the level of potential-temperature filaments, where divergence

hastens the contraction of warm filaments and slows the contraction of cold filaments. An example of this asymmetry is given in Fig. 12a,b, which shows that warm filaments are associated with convergence and cold filaments are associated with divergence. This asymmetry in the divergent flow produces surface cooling as cold air sinks and warm air rises in thermally direct circulations; the sense of these circulations, and of the asymmetry, is determined by the fact that turbulent flows stretch material lines and thus increase $|\nabla_H \theta^s|$ (frontogenesis). A fundamental result of sQG^{+1} frontogenetical circulations is a reduced center of mass in the fluid. This realistic effect is not captured by the QG and shallow-water equations.

We hypothesize that this divergent-flow asymmetry is the source of vortex population and structural asymmetries. For example, as illustrated in Fig 12c, when cyclonic vortices approach one another and are close to merging, the relatively cold patch of fluid that is pinched between them produces divergence, which opposes merger. Just the reverse happens for merging anticyclones, which pinch a warm patch of fluid that converges, favoring merger (Fig 12d). This merger asymmetry encourages anticyclones to build to larger scales, whereas cyclones are discouraged and tend to accumulate around a particular length scale at a given time. A theory that can predict the preferred cyclone scale as a function of time for a given Rossby number and initial condition remains an open and interesting problem for future work.

We further hypothesize that additional structural asymmetries are due to at least three effects. First, surface cooling and conservation of θ^s in the vortex cores imply that cyclones strengthen relative to anticyclones when their amplitude is measured against the mean ($\theta^s - \bar{\theta^s}$). Second, vortices persistently sweep cold filaments near their periphery, which leads to broad anticyclones and compact "plateau-like" cyclones. Third, these structural asymmetries may persist when perturbed, because they imply that vortex Rossby waves (e.g., Guinn and Schubert 1993; Montgomery and Kallenbach 1997) are trapped at the edge of cyclones, which gives cyclones an elliptical appearance as these waves propagate around the vortex.

In contrast, broad anticyclones support radial propagation and, ultimately, these waves break at the edge of the vortex, further contributing to broad structure.

Future work is needed to address these hypotheses, and also to link this work with earlier studies showing anticyclone dominance in flows strongly influenced by barotropic dynamics; sQG^{+1} dynamics represent a baroclinic two-dimensional limit in that they contain no barotropic (depth independent) velocity component. For example, Polvani et al. (1994) find that anticyclones are preferred over cyclones in shallow-water flow as the Froude number (ratio of fluid speed to gravity-wave speed) increases. They attribute this asymmetry to the smaller (larger) Rossby deformation radius for cyclones (anticyclones), which allows anticyclones to interact/merge more readily than cyclones. Arai and Yamagata (1994) show that isolated elliptical cyclones tend to eject more filamentary material during axisymmetrization when compared to anticyclones, and elliptical cyclones are also more prone to splitting. The anticyclone bias in shallow-water flow is strengthened on the β-plane due to a dispersion–nonlinearity balance that is not attainable to cyclones (e.g., Williams 1996). Yavneh et al. 1997 show that anticyclones also dominate in three-dimensional periodic f-plane simulations of the balance equations. In particular, anticyclones develop rapidly to larger horizontal scales (as in shallow water), which allows them to interact over deeper layers and collect into columnar vortices faster than cyclones.

A natural extension of the present work that links with studies of barotropically dominated flows involves the introduction of a second horizontal boundary; this addition allows barotropic flow to develop naturally, and promotes columnar organization on the largest scales. Because anticyclones build to larger scales faster than cyclones, we anticipate that anticyclones will be first to engage a partner on the opposing boundary, producing a barotropic structure; the vortex horizontal length scale for which this process begins is expected to depend on boundary separation. In the limit of infinite boundary separation, sQG^{+1} dynamics are recovered. For finite boundary separation larger scales will tend toward barotropy; how-

ever, there will always be scales short enough such that the opposing boundary is never felt and sQG^{+1} dynamics prevail. Exploration of these and similar problems should promote deeper understanding of the various regimes of cyclone–anticyclone asymmetry, and the role of barotropic motions in continuously stratified fluids.

Acknowledgments.

GJH acknowledges support through NSF Grant ATM-9980744. DJM acknowledges support through NSF DMR-9704724, DOE DE-FG02-88ER25053, the Alfred P. Sloan Foundation, and the NCAR Visiting Scientist program through the MMM Division. We thank Martin Juckes and an anonymous reviewer for comments that helped clarify portions of the manuscript.

Appendix A: Next-Order PV Inversion

Because the general QG^{+1} model is thoroughly discussed in Muraki et al. (1999), only the key results and simplifications relevant to the sQG^{+1} PV inversion are summarized here. The QG^{+1} approach replaces primitive variables (u, v, θ) with potentials (Φ, F, G), where

$$\begin{aligned} v &= \Phi_x - G_z \\ -u &= \Phi_y + F_z \\ \theta &= \Phi_z + G_x - F_y \ , \end{aligned} \tag{12}$$

and the continuity equation implies that

$$\epsilon\, w = F_x + G_y. \tag{13}$$

Next-order corrections in Rossby number are incorporated by expanding the potentials as the perturbation series

$$\begin{aligned} \Phi &\sim \Phi^0 + \epsilon\, \Phi^1 \\ F &\sim \epsilon\, F^1 \\ G &\sim \epsilon\, G^1 \ . \end{aligned} \tag{14}$$

For balanced states, these potentials are obtained by the solution of three-dimensional Poisson equations, subject to appropriate boundary conditions:

$$\begin{aligned} \nabla^2 \Phi^0 &= 0 \quad , & \Phi^{0s}_z &= \theta^s - \bar{\theta^s}; \\ \nabla^2 F^1 &= 2\, J(\Phi^0_z, \Phi^0_x) \quad , & F^{1s} &= 0; \\ \nabla^2 G^1 &= 2\, J(\Phi^0_z, \Phi^0_y) \quad , & G^{1s} &= 0; \\ \nabla^2 \Phi^1 &= |\nabla \Phi^0_z|^2 \quad , & \Phi^{1s}_z &\sim \bar{\theta^s}; \end{aligned} \tag{15}$$

where uniform (zero) PV has been assumed, and $\nabla^2 = \partial_{xx} + \partial_{yy} + \partial_{zz}$. The first equation in (15) has solution (7), which defines winds for sQG dynamics. Although the correction potentials (Φ^1, F^1, G^1) are determined by Poisson inversions of three-dimensional inhomogeneous

terms, we demonstrate the following surprising reduction to Laplace (surface) inversions. Using the fact that the inhomogeneous terms for (Φ^1, F^1, G^1) involve only Φ^0, which satisfies a Laplace problem, we may specify the following exact particular solutions:

$$\begin{aligned} F^1 &= \Phi^0_y \, \Phi^0_z &+ \tilde{F}^1 \\ G^1 &= -\Phi^0_x \, \Phi^0_z &+ \tilde{G}^1 \\ \Phi^1 &= \tfrac{1}{2}\Phi^0_z \, \Phi^0_z &+ \tilde{\Phi}^1. \end{aligned} \tag{16}$$

The homogeneous terms $(\tilde{F}^1, \tilde{G}^1, \tilde{\Phi}^1)$ satisfy a Laplace problem, with boundary conditions that allow (F^1, G^1, Φ^1) to satisfy (15):

$$\begin{aligned} \nabla^2 \tilde{F}^1 &= 0 \quad , \qquad \tilde{F}^{1s} &= -\Phi^0_y \, \Phi^0_z \\ \nabla^2 \tilde{G}^1 &= 0 \quad , \qquad \tilde{G}^{1s} &= \Phi^0_x \, \Phi^0_z \\ \nabla^2 \tilde{\Phi}^1 &= 0 \quad , \qquad \tilde{\Phi}^{1s}_z &\sim \bar{\theta}^s - \Phi^0_z \, \Phi^0_{zz} \, . \end{aligned} \tag{17}$$

Next-order surface winds may then be evaluated from

$$\begin{aligned} F^1_z &= (\Phi^0_y \, \Phi^0_z)_z &- \mathcal{F}^{-1}\left\{-|K|\mathcal{F}\left[\Phi^0_y \, \Phi^0_z\right]\right\} \\ G^1_z &= -(\Phi^0_x \, \Phi^0_z)_z &+ \mathcal{F}^{-1}\left\{-|K|\mathcal{F}\left[\Phi^0_x \, \Phi^0_z\right]\right\} \\ \Phi^1_x &= \Phi^0_{xz} \, \Phi^0_z &- \mathcal{F}^{-1}\left\{\tfrac{ik}{-|K|}\mathcal{F}\left[\bar{\theta}^s - \Phi^0_z \, \Phi^0_{zz}\right]\right\} \\ \Phi^1_y &= \Phi^0_{yz} \, \Phi^0_z &- \mathcal{F}^{-1}\left\{\tfrac{il}{-|K|}\mathcal{F}\left[\bar{\theta}^s - \Phi^0_z \, \Phi^0_{zz}\right]\right\}, \end{aligned} \tag{18}$$

where $\mathcal{F}^{-1}$ is the inverse Fourier transform. Note that the $(k, l) = (0, 0)$ contribution to Φ^1_x and Φ^1_y is $O(Ro^2)$ and is neglected.

Appendix B: Vortex Census Algorithm

Vortices are defined in terms of grid-point $\theta^s - \bar{\theta}^s$ since they are clearly distinguished from the background turbulence in that field. The vortex-census algorithm proceeds through the following steps.

1) At each grid point (i, j), determine whether $\theta^s(i, j) > \theta^s{}_{min}$, where $\theta^s{}_{min}$ is a lower bound that is useful in rejecting local maxima associated with filaments.

2) Determine whether grid point (i, j) represents a local maximum by searching outward along radial arms. The radial arms are separated azimuthally by 45°, so no interpolation is required. If any grid point (m, n) along any radial arm satisfies $\theta^s(m, n) > \theta^s(i, j)$, point (i, j) is rejected. The search along each arm stops successfully when $\theta^s(m, n) < \theta^s{}_{crit}$.

An additional filament filter is derived from the radial arms by computing the distance ("diameter") along four pairs of arms, where the pairs are selected as $(-x, -y)$ reflections through the vortex center; in the case of a circular vortex, these values are equal to the diameter. If any of the four diameter values falls below the threshold d_{min}, then the vortex is rejected.

3) The vortex centroid $(\bar{x}, \bar{y})$ is determined by first establishing a local mask that defines the vortex as $\theta^s > \theta^s{}_{crit}$. The mask is established by spiraling outward from (i, j) and setting all points where $\theta^s(m, n) < \theta^s{}_{crit}$ to zero; if the point adjacent to (m, n) and closer to (i, j) is zero, (m, n) is set to zero. The vortex centroid is then calculated by

$$\bar{x} = \frac{\sum_{m,n} x(m, n)\, \theta^s(m, n)}{\sum_{m,n} \theta^s(m, n)} \qquad\qquad \bar{y} = \frac{\sum_{m,n} y(m, n)\, \theta^s(m, n)}{\sum_{m,n} \theta^s(m, n)} \tag{19}$$

Merging vortices are filtered by requiring that $\{[\bar{x} - x(i, j)]^2 + [\bar{y} - y(i, j)]^2\}^{1/2} < r_{minor}/4$, where r_{minor} is the vortex minor-axis length scale as defined subsequently.

4) The vortex major- and minor-axis length scales are determined as moments about the centroid. A $2 \times N$ deviation matrix $\mathbf{X}$ is constructed for the N grid points defining the vortex. Entries in the first and second row of $\mathbf{X}$ are given by $\theta^s\,(m, n)^{1/2}\,[x(i, j) - \bar{x}]$ and

$\theta^s(m,n)^{1/2}\,[y(m,n)-\bar{y}]$, respectively. The 2×2 covariance matrix is defined as

$$\mathbf{S}=\left[\sum_{m,n}\theta^s(m,n)\right]^{-1}\mathbf{X}\mathbf{X}^{\mathbf{T}}. \tag{20}$$

The vortex major- and minor-axis length scales are defined in terms of the scaled eigenvalues of $\mathbf{S}$. For example, the major axis is given in terms of the leading eigenvalue, λ_1, as $(2\lambda_1)^{1/2}$.

The parameters used in this study are: ${\theta^s}_{min}=0.5$, ${\theta^s}_{crit}=\max\left[(\theta^s(i,j)\,e^{-2},\,0.4)\right]$, and $d_{min}=2.0$. These values were determined empirically, and appear to apply over a wide range of numerical resolution. Moreover, this tuning of the algorithm is conservative in that we noticed that it would occasionally omit a small, weak vortex, but it would never include a filament.

References

Arai, M., and T. Yamagata, 1994: Asymmetric evolution of eddies in rotating shallow water. *Chaos*, **4,** 163–175.

Blumen, W., 1978: Uniform potential vorticity flow: Part 1. Theory of wave interactions and two-dimensional turbulence. *J. Atmos. Sci.*, **35,** 774-789.

Bracco, A., J. C. McWilliams, G. Murante, A. Provenzale, and J. B. Weiss, 2000: Revisiting freely decaying two-dimensional turbulence at millennial resolution. *Phys. Fluids*, **12,** 2931–2941.

Charney, J. G., 1971: Geostrophic turbulence. *J. Atmos. Sci.*, **28,** 1087–1094.

Cushman-Roisin, B., and B. Tang, 1990: Geostrophic turbulence and emergence of eddies beyond the radius of deformation. *J. Phys. Oceanogr.*, **20,** 97–113.

Davies, H. C., and J. C. Müller, 1988: Detailed description of deformation-induced semi-geostrophic frontogenesis. *Quart. J. Roy. Meteor. Soc.*, **114,** 1201–1219.

Durran, D. R., 1999: *Numerical methods for wave equations in geophysical fluid dynamics.* Springer–Verlag, 465 pp.

Guinn, T. A., and W. H. Schubert, 1993: Hurricane spiral bands. *J. Atmos. Sci.*, **50,** 3380–3403.

Hakim, G. J., 2000: Climatology of coherent structures on the extratropical tropopause. *Mon. Wea. Rev.*, **128,** 385–406.

Herring, J. R., R. M. Kerr, and R. Rotunno, 1994: Ertel's potential vorticity in unstratified turbulence. *J. Atmos. Sci.*, **51,** 35–47.

Held, I. M., R. T. Pierrehumbert, S. T. Garner, and K. L. Swanson, 1995: Surface quasi-geostrophic dynamics. *J. Fluid Mech.*, **282,** 1–20.

Hoskins, B. J., and F. P. Bretherton, 1972: Atmospheric frontogenesis models: Mathematical formulation and solution. *J. Atmos. Sci.*, **29,** 11–37.

Juckes, M., 1994: Quasigeostrophic dynamics of the tropopause. *J. Atmos. Sci.*, **51,** 2756–2768.

Juckes, M., 1995: Instability of surface and upper-tropospheric shear lines. *J. Atmos. Sci.*, **52,** 3247–3262.

Lumley, J. L., 1990: *Whither turbulence? Turbulence at the crossroads.* Springer-Verlag, 535 pp.

McWilliams, J. C., 1984: The emergence of isolated coherent vortices in turbulent flow. *J. Fluid Mech.*, **146,** 21–43.

McWilliams, J. C., 1989: Statistical properties of decaying geostrophic turbulence. *J. Fluid Mech.*, **198,** 199–230.

McWilliams, J. C., 1990a: The vortices of two-dimensional turbulence. *J. Fluid Mech.*, **219,** 361–385.

McWilliams, J. C., 1990b: The vortices of geostrophic turbulence. *J. Fluid Mech.*, **219,** 387–404.

McWilliams, J. C., J. B Weiss, and I. Yavneh, 1999: The vortices of homogeneous geostrophic turbulence. *J. Fluid Mech.*, **401,** 1–26.

Montgomery, M. T. and R. J. Kallenbach, 1997: A theory for vortex Rossby-waves and its

application to spiral bands and intensity changes in hurricanes.
Quart. J. Roy. Meteor. Soc., **123,** 435–465.

Muraki, D. J., C. Snyder, and R. Rotunno, 1999: The next-order corrections to quasigeostrophic theory. *J. Atmos. Sci.*, **56,** 1547–1560.

Muraki, D. J., and G. J. Hakim, 2001: Balanced asymmetries of waves on the tropopause. *J. Atmos. Sci.*, **58,** 237–252.

Pedlosky, J., 1987: *Geophysical Fluid Dynamics.* 2nd ed. Springer–Verlag, 710 pp.

Polvani, L. M., J. C. McWilliams, M. A. Spall, and R. Ford, 1994: The coherent structures of shallow-water turbulence: Deformation-radius effects, cyclone/anticyclone asymmetry and gravity-wave generation. *Chaos*, **4,** 177–186.

Rivest, C., C. A. Davis, and B. F. Farrell, 1992: Upper-tropospheric synoptic-scale waves. Part I: Maintenance as Eady normal modes. *J. Atmos. Sci.*, **49,** 2108– 2119.

Salmon, R., 1998: *Lectures on geophysical fluid dynamics.* Oxford University Press, 378 pp.

Sanders, F., 1988: Life history of mobile troughs in the upper westerlies. *Mon. Wea. Rev.*, **116,** 2629–2648.

Thorpe, A. J., 1986: Synoptic scale disturbances with circular symmetry. *Mon. Wea. Rev.*, **114,** 1384–1389.

Vallis, G. K., 1996: Potential vorticity inversion and balanced equations of motion for rotating and stratified flows. *Quart. J. Roy. Meteor. Soc.*, **122,** 291-322.

Warn, T., O. Bokhove, T. G. Shepherd, and G. K. Vallis, 1995: Rossby number expansions, slaving principles and balance dynamics. *Quart. J. Roy. Meteor. Soc.*, **121,** 723-729.

Williams, G. P., 1996: Jovian dynamics. Part 1: Vortex stability, structure, and genesis. *J. Atmos. Sci.*, **53,** 2685–2734.

Wirth, V., 2001: Cyclone–Anticyclone asymmetry concerning the height of the thermal and the dynamical tropopause. *J. Atmos. Sci.*, **58,** 26–37.

Yavneh, I., A. F. Shchepetkin, J. C. McWilliams, and L. P. Graves, 1997: Multigrid solutions of rotating, stably stratified flows: The balance equations and their turbulent dynamics. *J. Comput. Phys.*, **136,** 245–262.

Figure Captions

Figure 1. Surface potential temperature evolution for numerical solutions of sQG^{+1} [panels (b) and (c)] and sQG [panel (d)] freely decaying turbulence. The random initial condition shown in (a) evolves into a field of vortices and filaments by $t = 200$ (b). By $t = 1000$, cyclone–anticyclone asymmetries and surface cooling are prominent in the sQG^{+1} solution (c), and are absent in the sQG solution (d). All units are non-dimensional, and the Rossby number (ϵ) is 0.1 for the sQG^{+1} solution.

Figure 2. (a) Mean surface potential temperature, $\bar{\theta^s}$, as a function of nondimensional time. Dashed lines show ± 1 ensemble standard deviation about the ensemble mean (bold line). (b) Potential-temperature PDF at $t = 1000$ for sQG^{+1} (thick line) and sQG (thin line). Vertical lines show ± 1 ensemble standard deviation around the ensemble mean.

Figure 3. Ensemble-mean surface potential-temperature variance spectra. The sQG curve (dashed line) has been displaced from the sQG^{+1} curve (solid line) for clarity. Thin vertical lines show ± 1 ensemble standard deviation around the ensemble mean, and lines with slopes of $-5/3$ and -1 are provided for reference. The spectral peak in the initial condition is denoted by the bold arrow.

Figure 4. $t = 1000$ ensemble-mean PDF for perturbation surface potential temperature [$(\theta^s - \bar{\theta^s})$, lower panel] and surface divergence (solid) and leading-order deformation magnitude (dashed) as a function of $\theta^s - \bar{\theta^s}$. Thin solid vertical lines show ± 1 ensemble standard deviation around the ensemble mean, and the thin dashed vertical line denotes the peak of the $\theta^s - \bar{\theta^s}$ PDF; note that this is a skewed distribution.

Figure 5. Ensemble-mean PDFs for (a) surface potential temperature, $\theta^s - \bar{\theta^s}$, and (b) vorticity, and joint PDFs of surface potential temperature, $\theta^s - \bar{\theta^s}$, and vorticity for (c) sQG^{+1} and (d) sQG. In (a) and (b), values for $\theta^s - \bar{\theta^s} < 0$ have been folded across the

origin, with positive values given by thick solid lines and negative values given by thick dashed lines; the symmetric sQG curve is given by a thin solid line. Thin vertical lines show ± 1 ensemble standard deviation around the ensemble mean. Contours in (c) and (d) are given in powers of 10, with an innermost contour of 0.1

Figure 6. Vortex census data at $t = 1000$ showing ensemble-mean vortex amplitude (a, b) and radius (c, d); note that vortex amplitude is defined relative to $\bar{\theta}^s$. sQG^{+1} solutions are given in (a, c) and sQG solutions are given in (b, d). Thin vertical lines show ± 1 ensemble standard deviation around the ensemble mean, which is given by the bold solid line.

Figure 7. Vortex radius as a function of amplitude, $\theta^s - \bar{\theta}^s$, for sQG^{+1} (a) and sQG (b) solutions at $t = 1000$. Each vortex is represented by a dot, and the solid lines are constant-density contours (.005 .01 .02 .03) of the joint PDF.

Figure 8. Vortex number as a function of time. The thin dashed line represents sQG vortices, the thick solid line represents sQG^{+1} cyclones, and the thick dashed line represents sQG^{+1} anticyclones. A solid line with slope $-.55$ is provided for reference.

Figure 9. $t = 1000$ ensemble-mean PDFs for magnitude of the horizontal gradient of surface potential temperature, conditioned on $|\theta^s - \bar{\theta}^s| > 1$. Cyclonic sQG^{+1} (positive) values are given by thick solid lines and anticyclonic sQG^{+1} (negative) values are given by thick dashed lines; the symmetric sQG curve is given by a thin solid line. Short vertical lines show ± 1 ensemble standard deviation around the ensemble mean.

Figure 10. Vertical component of relative vorticity at $t = 1000$ for (a) sQG^{+1} and (b) sQG solutions. The vorticity shown in (b) is leading-order only, whereas in (a) the vorticity is correct to $0(\epsilon)$. (a) corresponds to the upper left quadrant of Fig. 1c, and (b) corresponds to the lower left quadrant of Fig. 1d.

Figure 11. Schematic illustration of the divergent-flow response to (a) cold and (b) warm filaments in deformation. Black arrows show the ambient deformation that acts to thin the filaments (thick grey lines) and provoke the divergent response in the vertical plane normal to the filaments (arrow heads and arrow tails). The net affect of the divergent motions, given by the grey arrows, is to accelerate the contraction of warm filaments relative to cold filaments.

Figure 12. Surface potential temperature (colors) and divergence (black lines) for examples of: (a) warm filaments; (b) cold filaments; (c) merging cyclones; and (d) merging anticyclones. Solid lines show divergence and dashed lines show convergence.

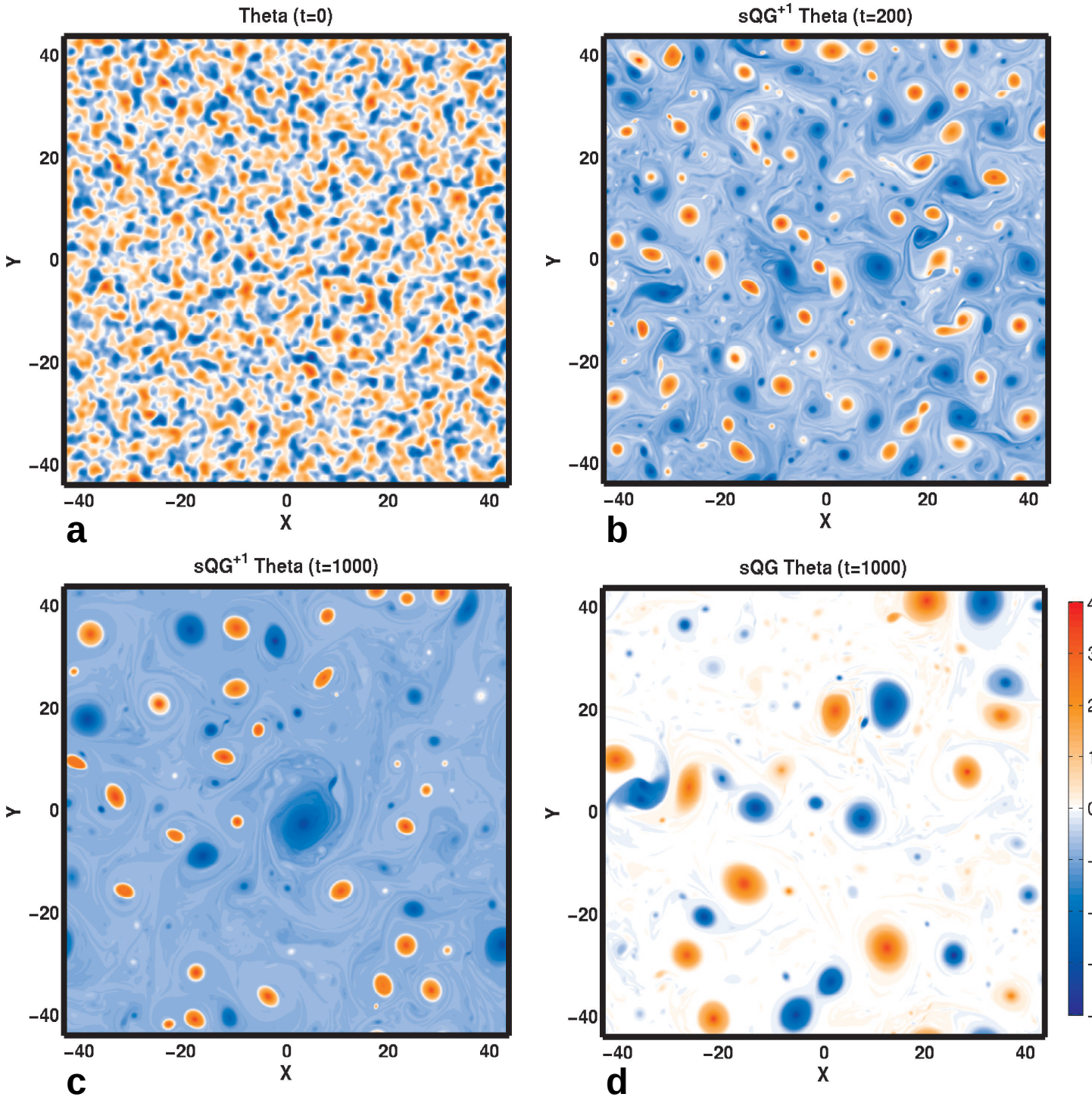

Figure 1: Surface potential temperature evolution for numerical solutions of sQG^{+1} [panels (b) and (c)] and sQG [panel (d)] freely decaying turbulence. The random initial condition shown in (a) evolves into a field of vortices and filaments by $t = 200$ (b). By $t = 1000$, cyclone–anticyclone asymmetries and surface cooling are prominent in the sQG^{+1} solution (c), and are absent in the sQG solution (d). All units are non-dimensional.

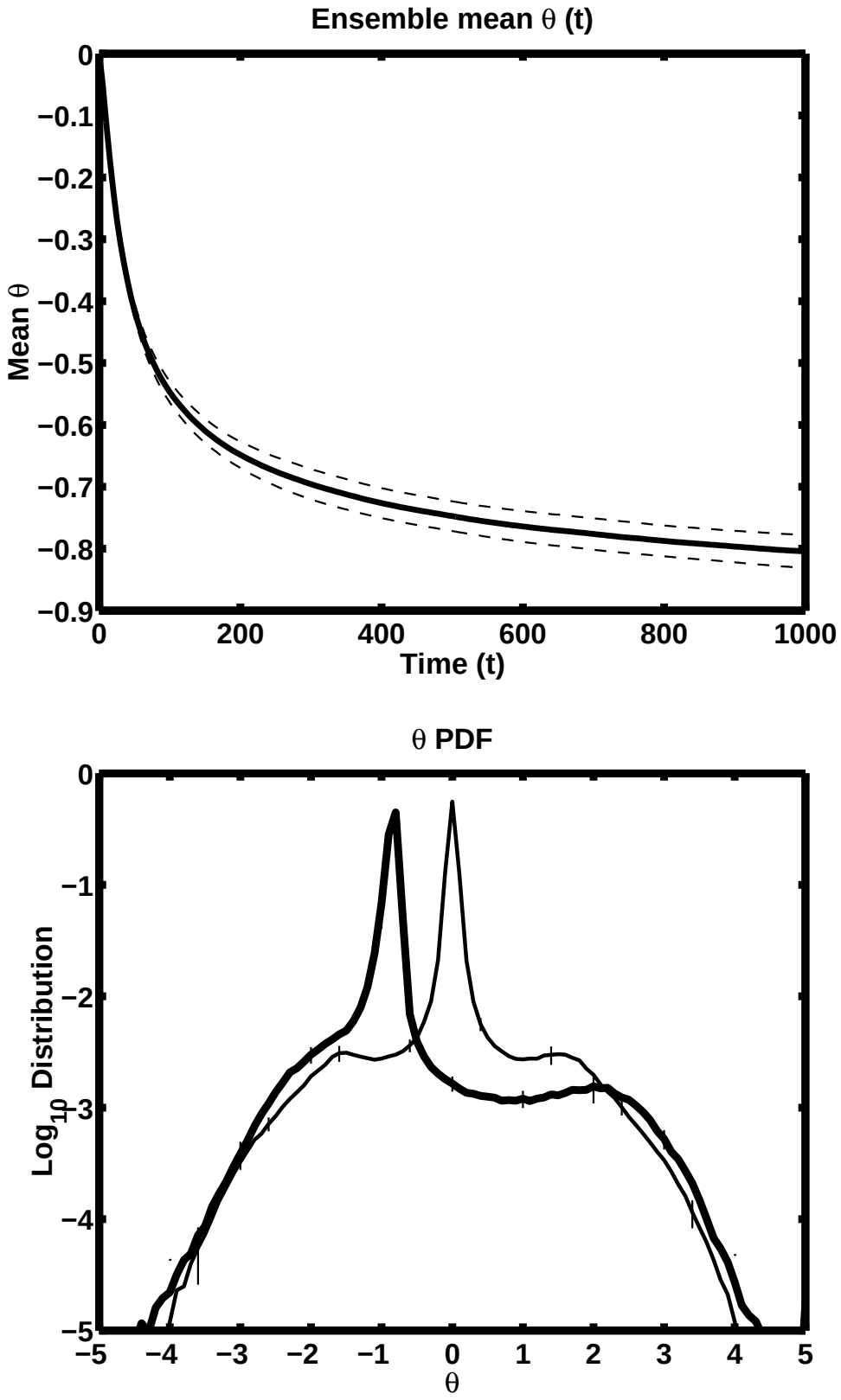

Figure 2: (a) Mean surface potential temperature, $\bar{\theta}^s$, as a function of nondimensional time. Dashed lines show ± 1 ensemble standard deviation about the ensemble mean (bold line). (b) Potential-temperature PDF at $t = 1000$ for sQG^{+1} (thick line) and sQG (thin line). Vertical lines show ± 1 ensemble standard deviation around the ensemble mean.

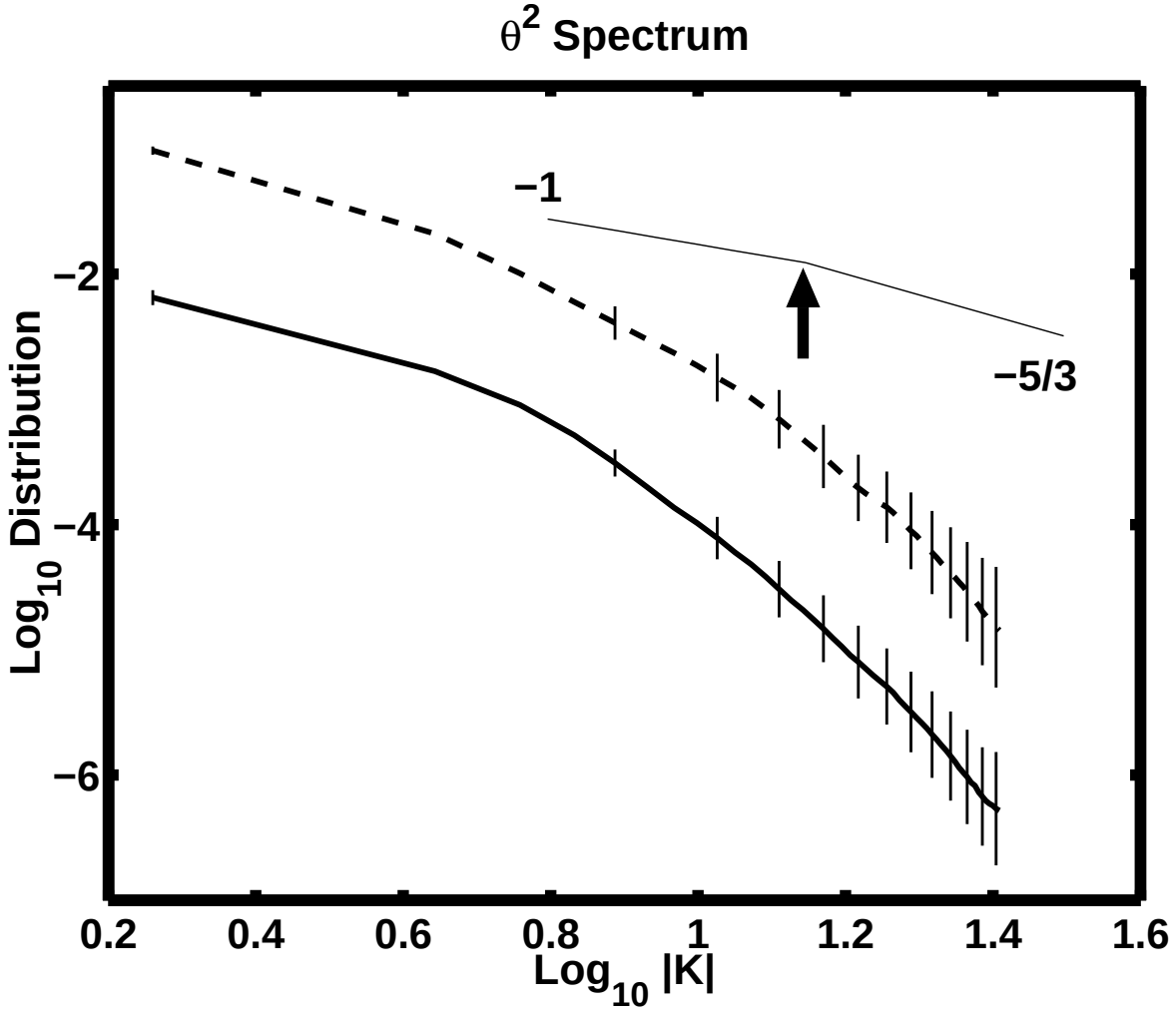

Figure 3: Ensemble-mean surface potential-temperature variance spectra. The sQG curve (dashed line) has been displaced from the sQG^{+1} curve (solid line) for clarity. Thin vertical lines show ± 1 ensemble standard deviation around the ensemble mean, and lines with slopes of $-5/3$ and -1 are provided for reference. The spectral peak in the initial condition is denoted by the bold arrow.

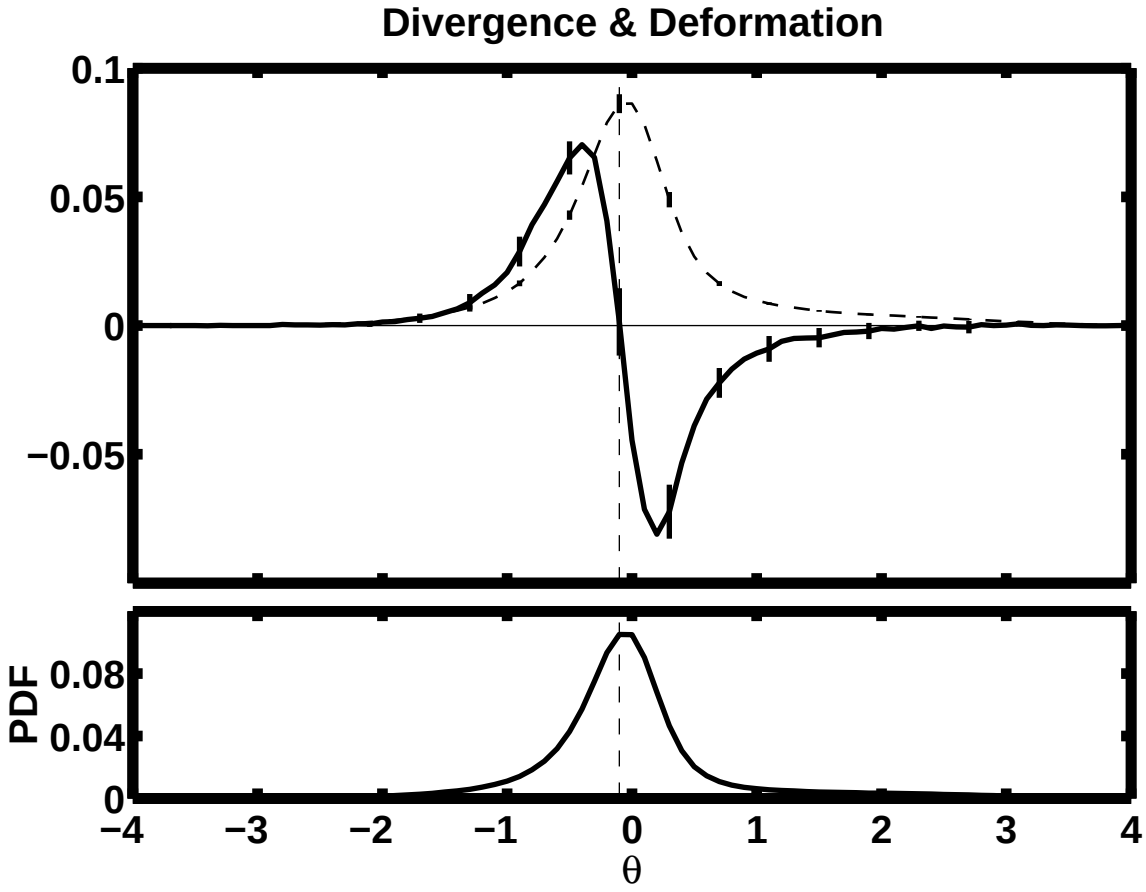

Figure 4: $t = 1000$ ensemble-mean PDF for perturbation surface potential temperature [$(\theta^s - \bar{\theta^s})$, lower panel] and surface divergence and total deformation magnitude as a function of $\theta^s - \bar{\theta^s}$. Thin solid vertical lines show ± 1 ensemble standard deviation around the ensemble mean, and the thin dashed vertical line denotes the peak of the $\theta^s - \bar{\theta^s}$ PDF; note that this is a skewed distribution.

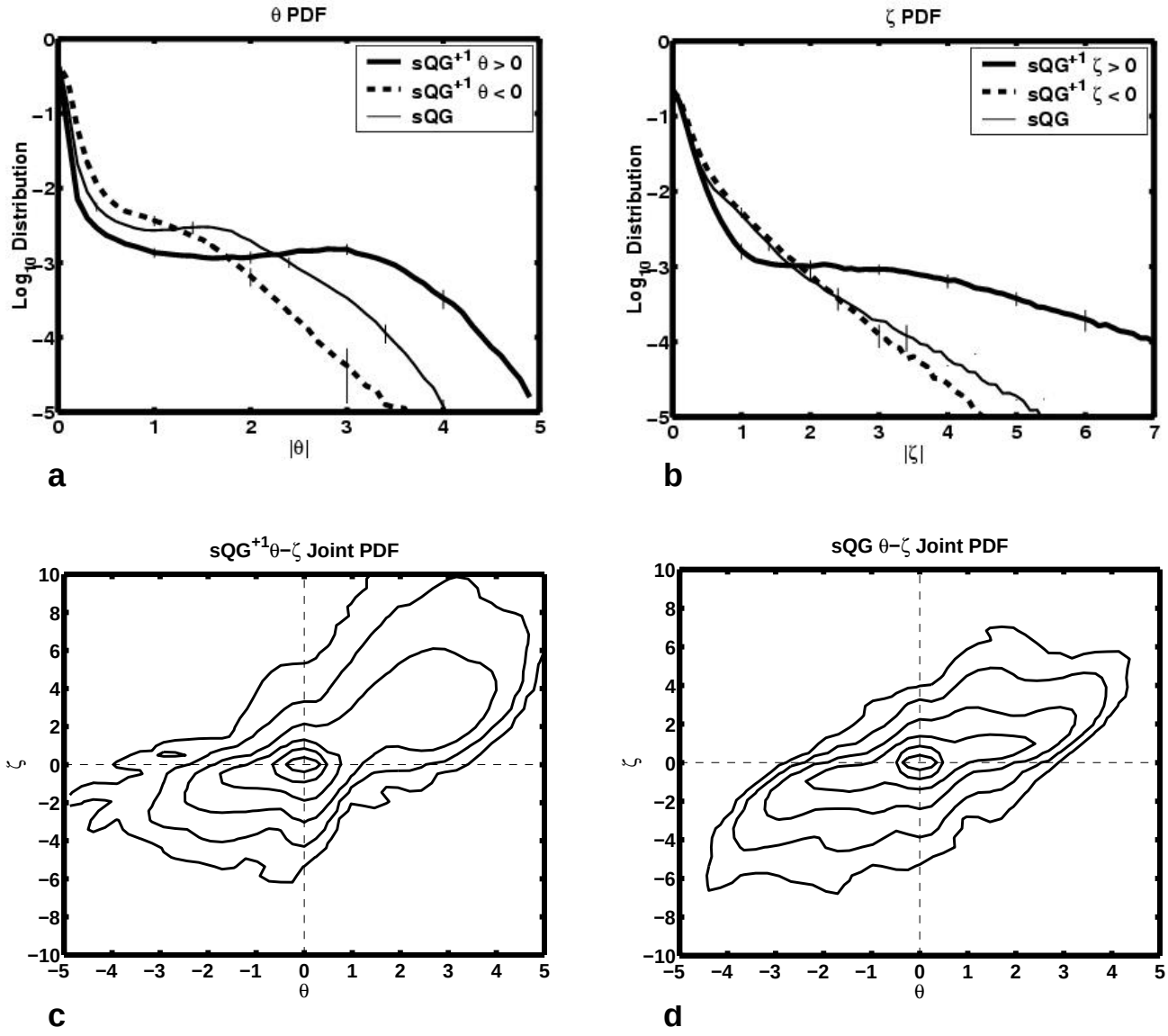

Figure 5: Ensemble-mean PDFs for (a) surface potential temperature, $\theta^s - \bar{\theta^s}$, and (b) vorticity, and joint PDFs of surface potential temperature, $\theta^s - \bar{\theta^s}$, and vorticity for (c) sQG^{+1} and (d) sQG. In (a) and (b), values for $\theta^s - \bar{\theta^s} < 0$ have been folded across the origin, with positive values given by thick solid lines and negative values given by thick dashed lines; the symmetric sQG curve is given by a thin solid line. Thin vertical lines show ± 1 ensemble standard deviation around the ensemble mean. Contours in (c) and (d) are given in powers of 10, with an innermost contour of 0.1

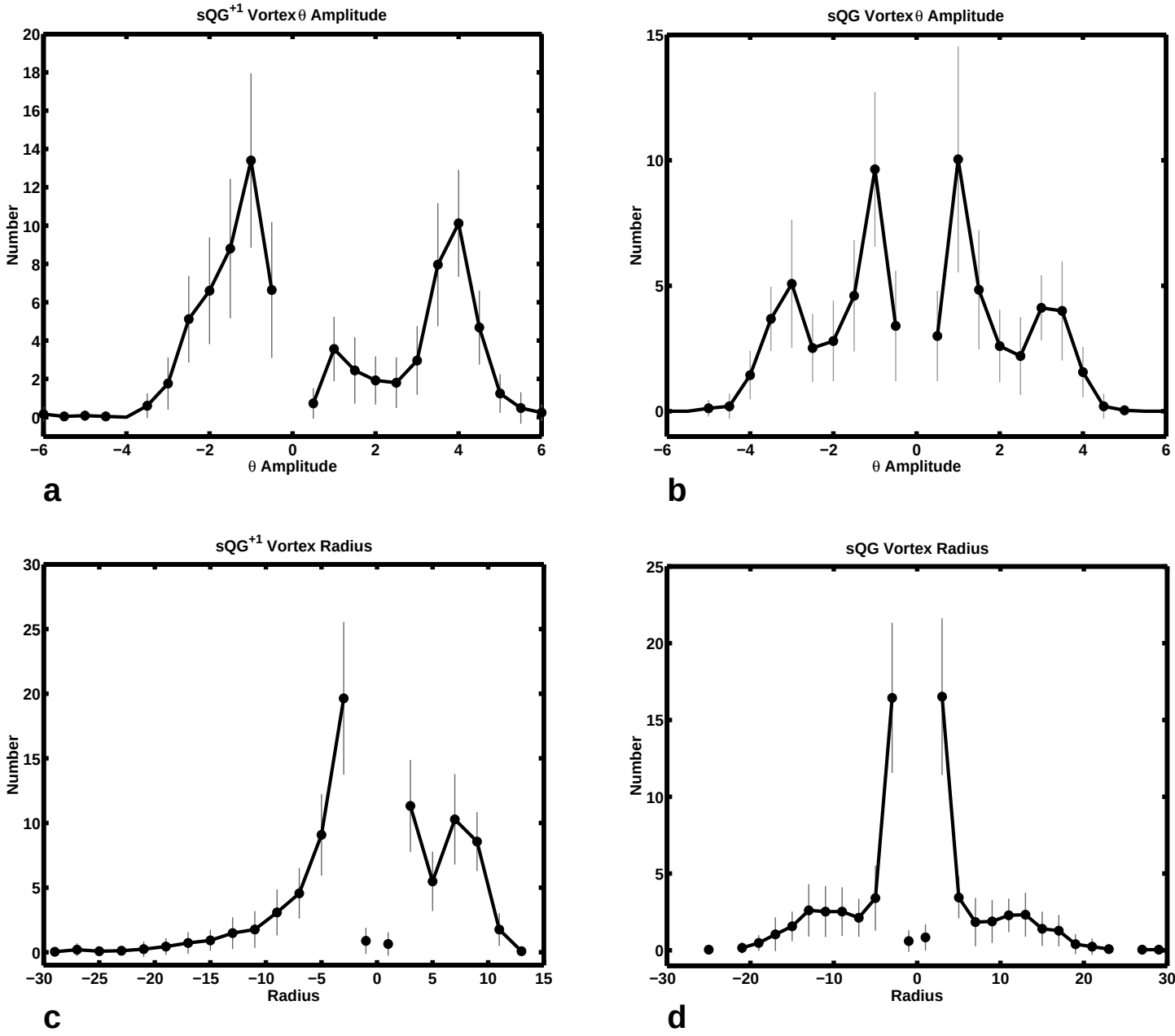

Figure 6: Vortex census data at $t = 1000$ showing ensemble-mean vortex amplitude (a, b) and radius (c, d); note that vortex amplitude is defined relative to $\bar{\theta}^s$. sQG^{+1} solutions are given in (a, c) and sQG solutions are given in (b, d). Thin vertical lines show ± 1 ensemble standard deviation around the ensemble mean, which is given by the bold solid line.

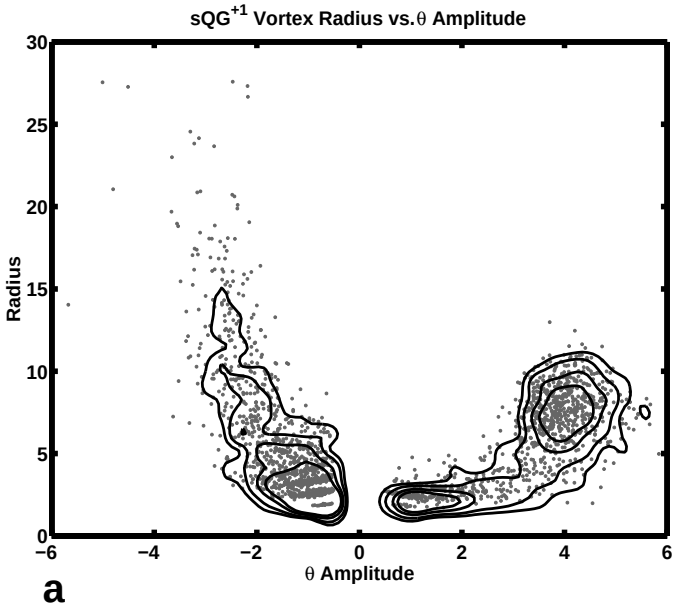

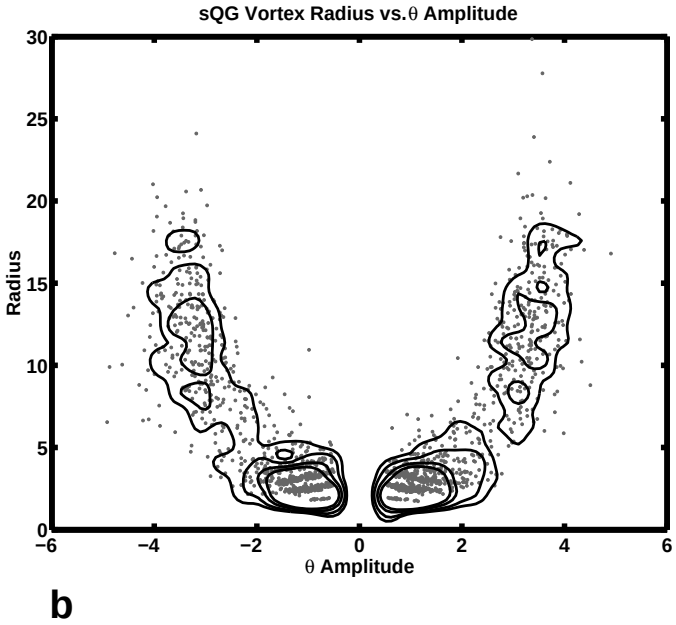

Figure 7: Vortex radius as a function of amplitude, $\theta^s - \bar{\theta}^s$, for sQG^{+1} (a) and sQG (b) solutions at $t = 1000$. Each vortex is represented by a dot, and the solid lines are constant-density contours (.005 .01 .02 .03) of the joint PDF.

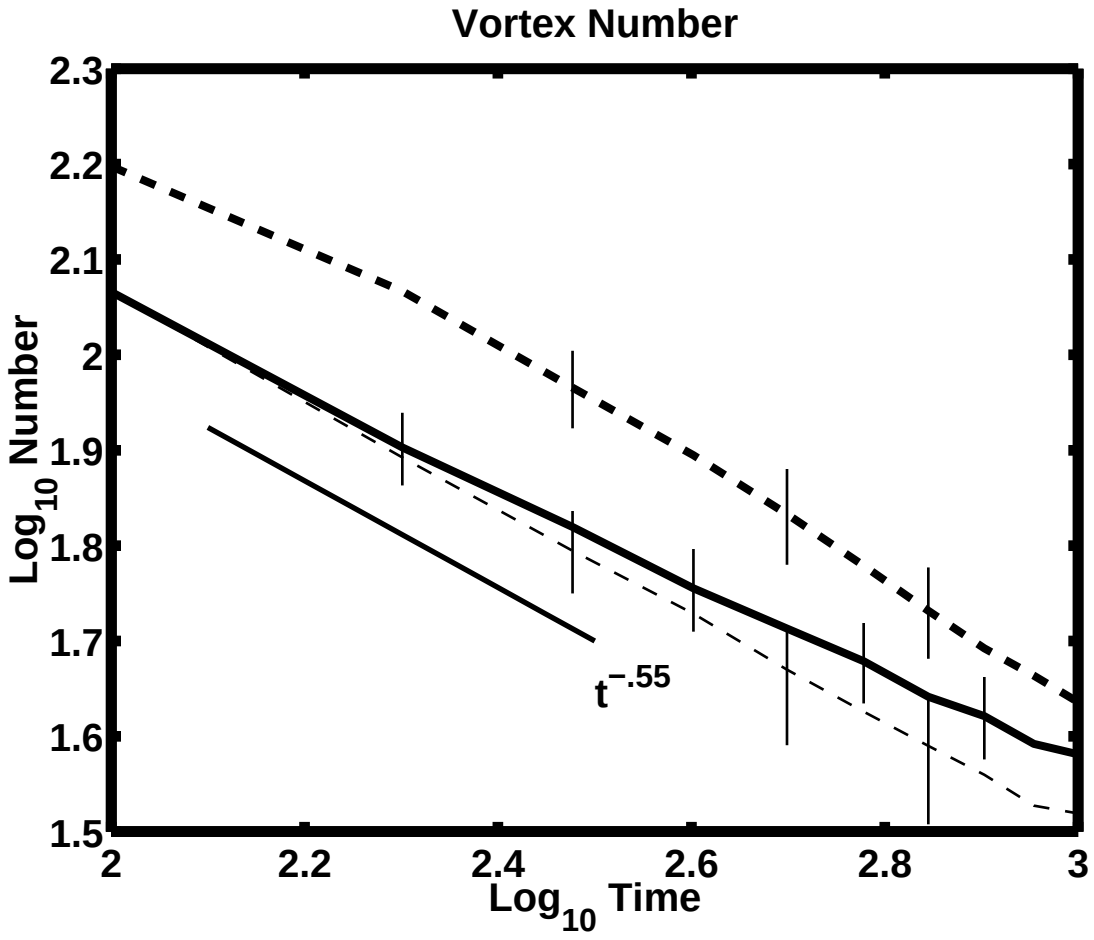

Figure 8: Vortex number as a function of time. The thin dashed line represents sQG vortices, the thick solid line represents sQG^{+1} cyclones, and the thick dashed line represents sQG^{+1} anticyclones. A solid line with slope $-.55$ is provided for reference.

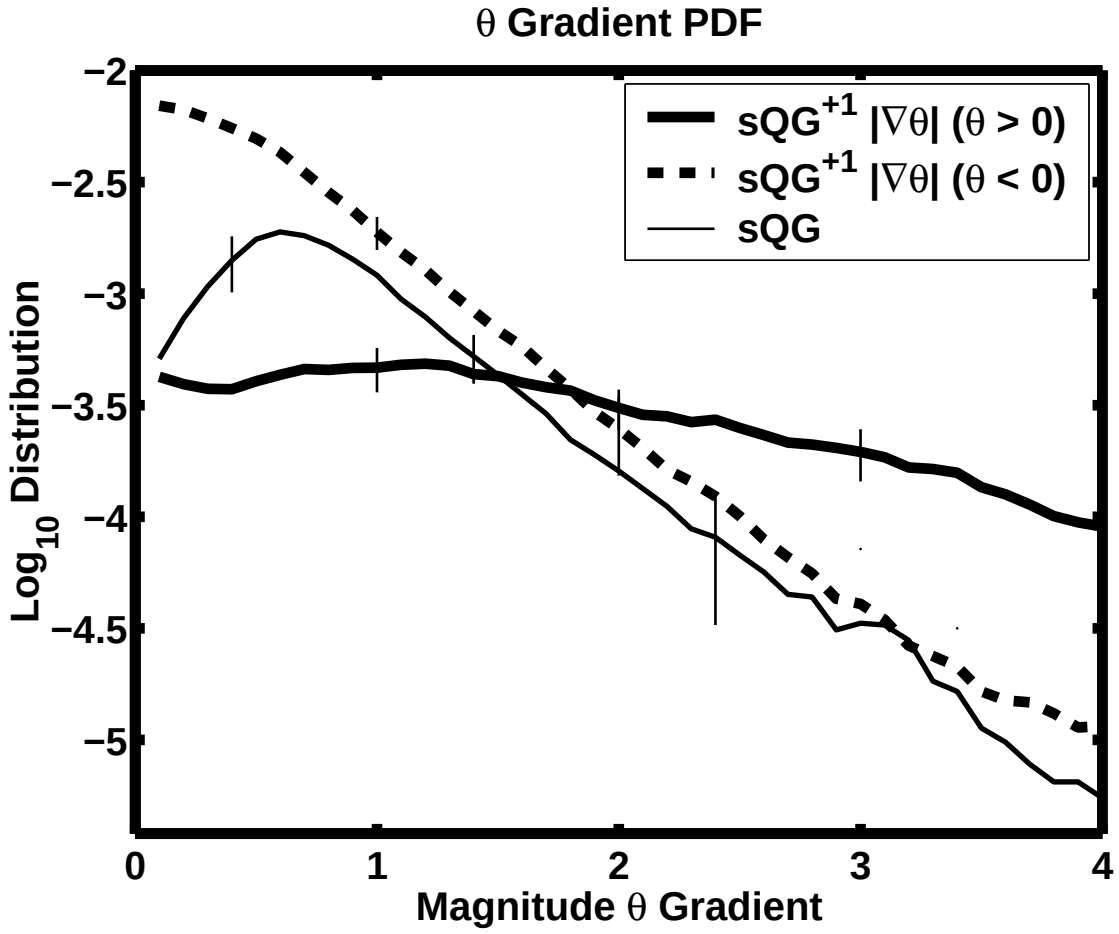

Figure 9: $t = 1000$ ensemble-mean PDFs for magnitude of the horizontal gradient of surface potential temperature, conditioned on $|\theta^s - \bar{\theta}^s| > 1$. Cyclonic sQG^{+1} (positive) values are given by thick solid lines and anticyclonic sQG^{+1} (negative) values are given by thick dashed lines; the symmetric sQG curve is given by a thin solid line. Short vertical lines show ± 1 ensemble standard deviation around the ensemble mean.

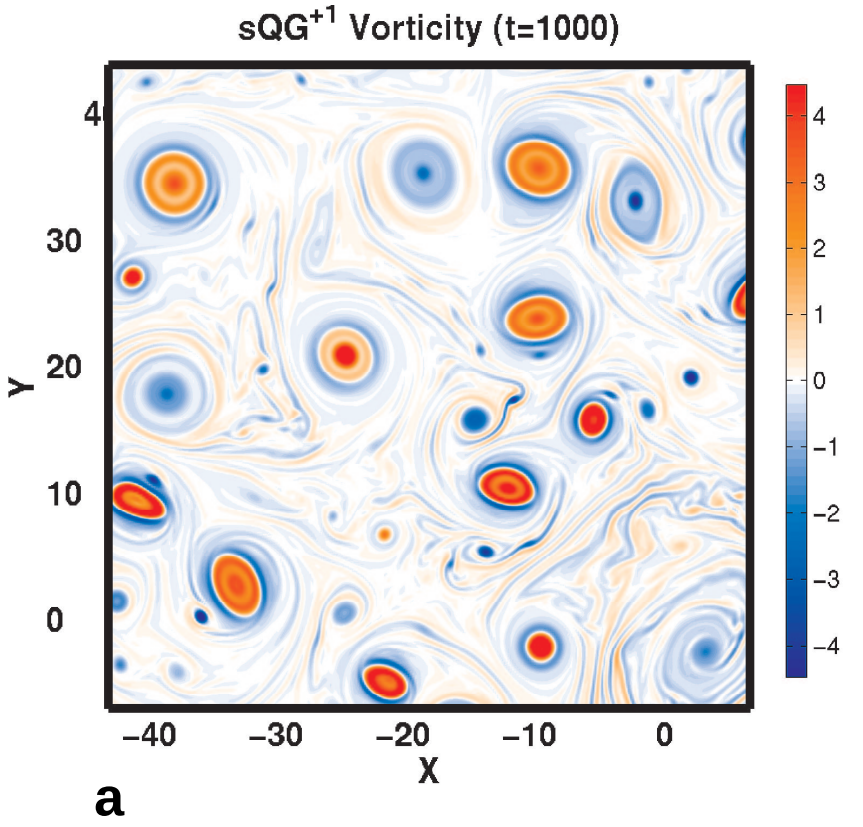

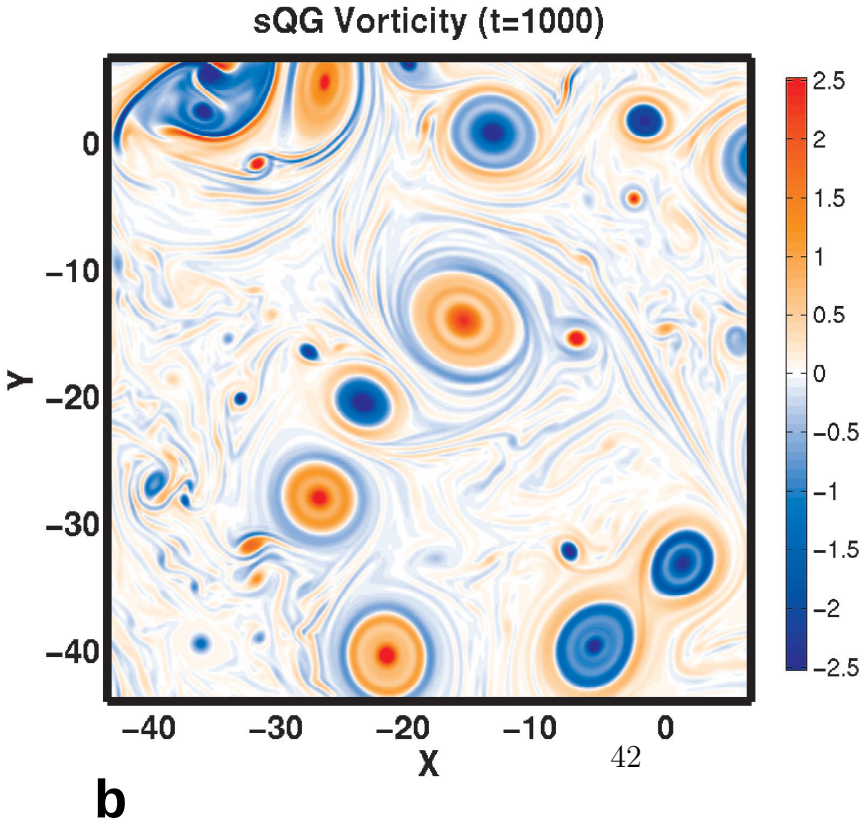

Figure 10: Vertical component of relative vorticity at $t = 1000$ for (a) sQG^{+1} and (b) sQG

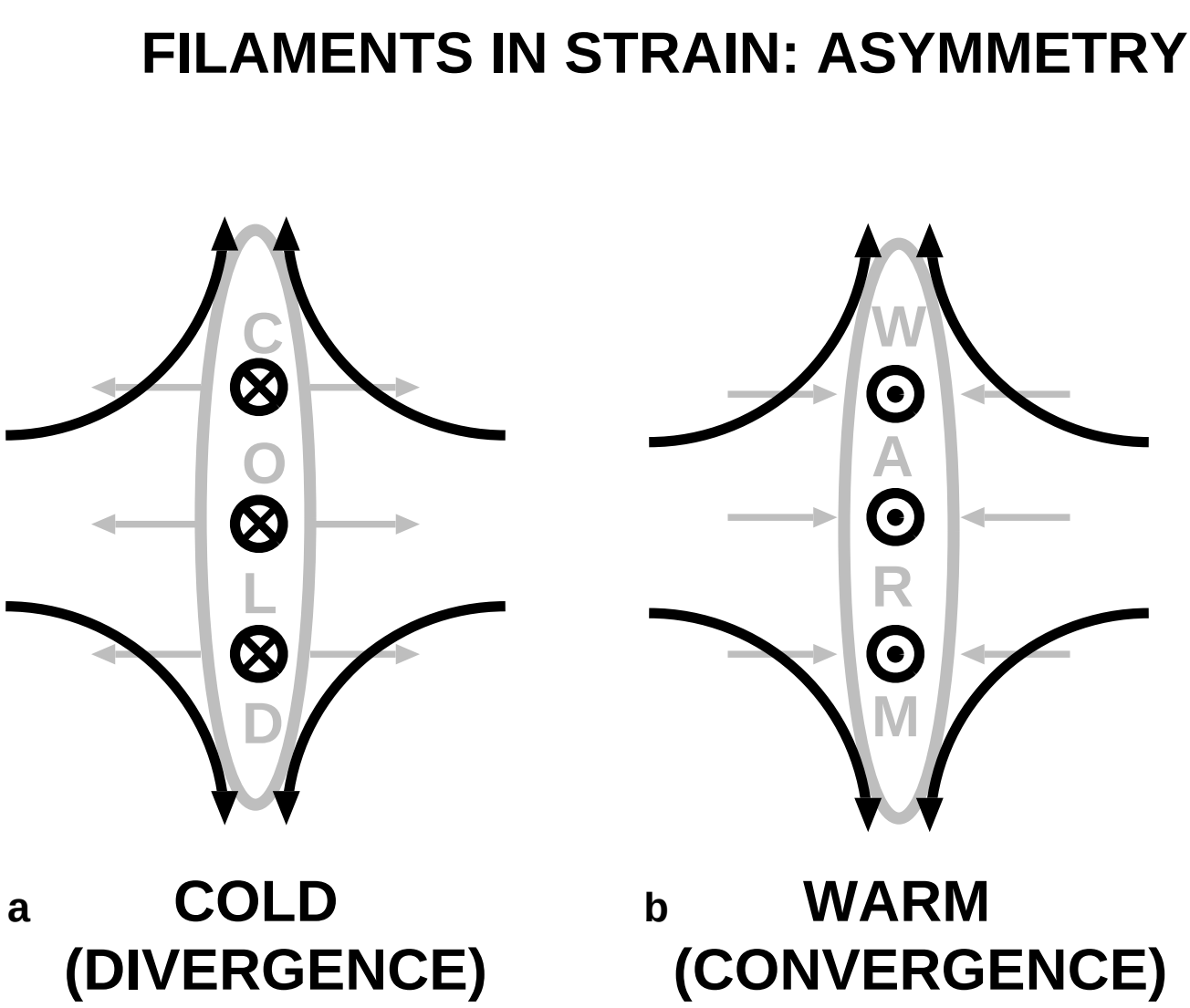

Figure 11: Schematic illustration of the divergent-flow response to (a) cold and (b) warm filaments in deformation. Black arrows show the ambient deformation that acts to thin the filaments (thick grey lines) and provoke the divergent response in the vertical plane normal to the filaments (arrow heads and arrow tails). The net affect of the divergent motions, given by the grey arrows, is to accelerate the contraction of warm filaments relative to cold filaments.

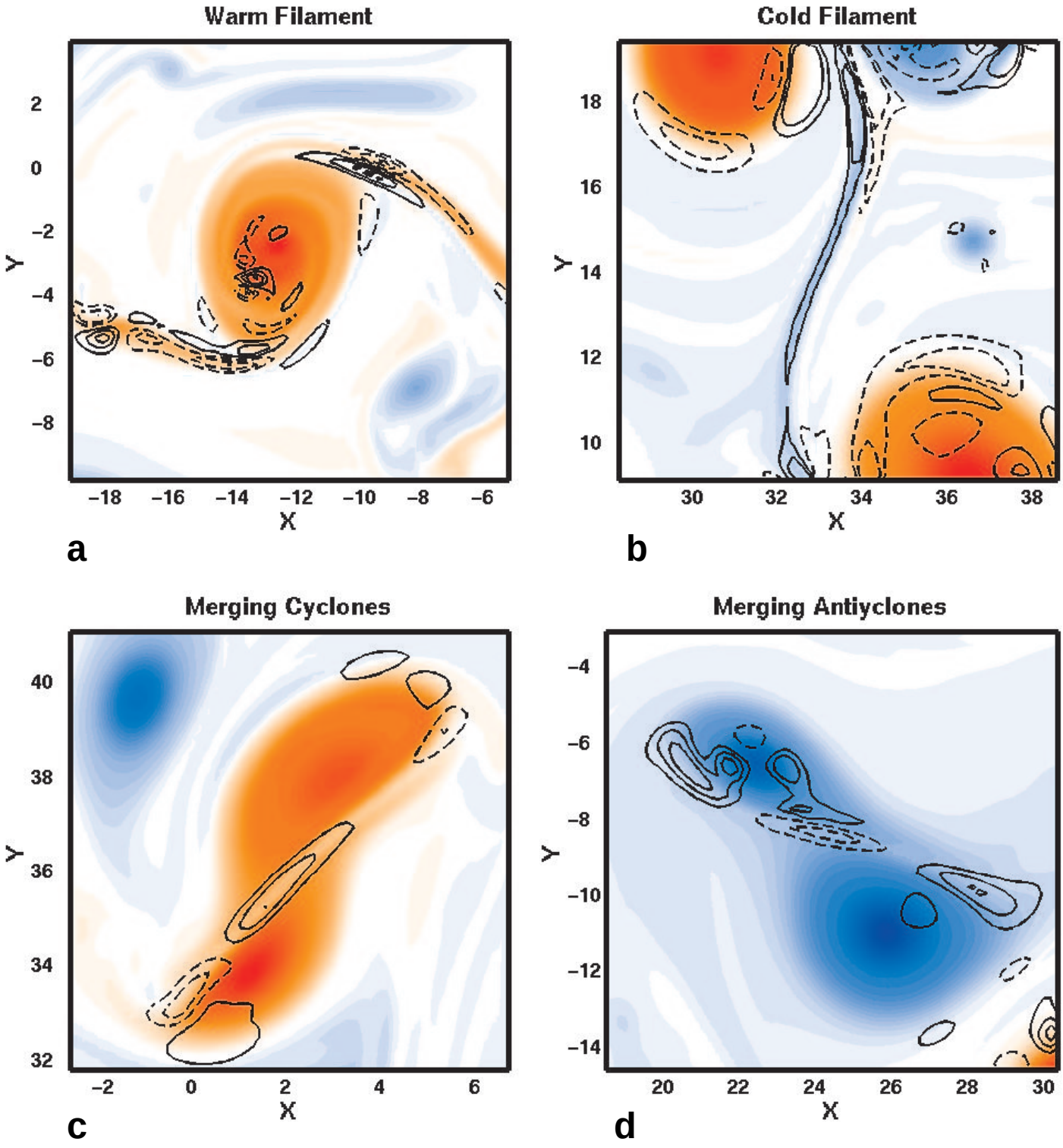

Figure 12: Surface potential temperature (colors) and divergence (black lines) for examples of: (a) warm filaments; (b) cold filaments; (c) merging cyclones; and (d) merging anticyclones. Solid lines show divergence and dashed lines show convergence.